

# Reversing a heavy-ion collision

Mikhail Stephanov<sup>1,2</sup> and Yi Yin<sup>1</sup>

<sup>1</sup>*Physics Department, University of Illinois at Chicago, Chicago, IL, 60607*

<sup>2</sup>*Enrico Fermi Institute, University of Chicago, Chicago, IL 60637*

(Dated: May 31, 2021)

We introduce a novel approach to study the longitudinal hydrodynamic expansion of the quark-gluon fluid created in heavy-ion collisions. It consists of two steps: First, we apply the *maximum entropy method* to reconstruct the freeze-out surface from experimentally measured particle distribution. We then take the output of the reconstruction as the “initial” condition to evolve the system *back* in time by solving the 1 + 1 ideal hydrodynamic equations *analytically*, using the method of Khalatnikov and Landau. We find an approximate Bjorken-like plateau in the energy density vs rapidity profile at the early times, which shrinks with time as the boundary shocks propagate inward. In Bjorken frame, the fluid velocity is close to zero within the plateau, as in the Bjorken solution, but increases outside the plateau. The results carry implications for fully numerical hydrodynamic simulations as well as models of heavy-ion collisions based on gauge-gravity duality.

## I. INTRODUCTION

In 1983, Bjorken proposed to describe the central region of the ultra-relativistic heavy-ion collisions by a boost-invariant solution of the hydrodynamic equations [1]. In this elegant solution, the fluid remains homogeneous and at rest in the Bjorken’s coordinates. The expansion of the system is entirely encoded in the expanding nature of the hyperbolic Bjorken coordinates, very similar to the Hubble expansion, but in one dimension. A direct implication of such boost-invariance at late times would be a mid-rapidity plateau in the particle production. Such a plateau is not apparent at RHIC [2, 3] or LHC [4] (see Fig. 1 below). Experimental results suggest that it is imperative to study longitudinal expansion beyond boost-invariant Bjorken model.

Fully numerical 1 + 1 [5, 6] and 3 + 1 [7, 8] relativistic hydrodynamic simulations are appropriate tools to address this challenge. Unlike the highly-symmetric idealized Bjorken model, in which the unknown initial condition is characterized by a single number (energy density, or initial time), a more realistic simulation requires much more information about the initial density and flow profile. While the initial profile of the fireball in the *transverse plane* has been studied extensively, our knowledge in longitudinal direction is comparatively poor. In practice, all the above simulations [5–8], rely on an ansatz with several free parameters for the initial profile. Those free parameters are tuned to match multiplicity distributions obtained as a result of the simulations to the experimental data. This “trial and error” method of determining the initial conditions is clearly computationally intensive.

In this paper we introduce a novel approach to determine the longitudinal hydrodynamic flow profile of the fireball created in heavy-ion collisions. It features two main ingredients which distinguishes it from the traditional approaches. First, we use the experimental data directly as an input to determine the hydrodynamic variables on the freeze-out surface. Second, we evolve the

system *back* in time using the freeze-out as “initial” condition. We are able to perform the evolution *analytically*.

Correspondingly, our approach involves two key steps. First, we apply the maximum entropy method (MEM) [9, 10] to invert Cooper-Frye freeze-out [11] prescription relating the hydrodynamic variables at the freeze-out hypersurface to the rapidity-dependent hadron spectrum measured in the experiments. As a state-of-the-art deconvolution technique, the maximum entropy method (MEM) has proven to be a powerful tool in other branches of physics [9, 12], including lattice QCD [13] and cosmology [14]. To the best of our knowledge, however, this is the first time that MEM has been applied to the physics of heavy-ion collisions.

In the second step, we take advantage of the fact that 1+1 ideal hydrodynamic equations with initial conditions given on the isothermal surface can be solved analytically. Since the ideal hydrodynamic equations are deterministic, we can evolve the system from freeze-out temperature to early times with the information of freeze-out surface we obtained in the first step. As a result, we are able to reconstruct the history of the longitudinal expansion and infer the longitudinal profile of the fireball at early times.

We find that, while the observed particle distribution does not show a rapidity plateau, the reconstructed hydrodynamic flow did have a rapidity plateau at earlier times. The width of the plateau shrinks with time as the boundary shocks propagate towards the center of the fireball.

This paper is organized as follows. In Sec. II, we discuss the deconvolution of Cooper-Frye freeze-out using the maximum entropy method. In Sec. III, we review the general solution of 1 + 1 ideal hydrodynamics. Our results are presented in Sec. IV. We show the reconstructed freeze-out surface obtained in the first step in subsection IV A. We then show the history of longitudinal expansion in subsection IV B. We compare the resulting early-time profile with that used in hydrodynamic simulations. Finally, in Sec. V, we conclude.

## II. RECONSTRUCTION OF FREEZE-OUT SURFACE AND MAXIMUM ENTROPY METHOD

We shall follow the standard Cooper-Frye approach [11] to relate the momentum-space multiplicity distribution  $d^3N_s/d^3p$  of the hadrons of a given species to the temperature  $T$  and flow velocity  $u^\mu$  profiles on the freeze-out hyper-surface:

$$p^0 \frac{d^3N_s}{d^3p} = \frac{1}{(2\pi)^3} p^\mu \int d^3\sigma_\mu(x) f(p; u(x), T(x)), \quad (1)$$

where  $f(p; u(x), T(x))$  is the local equilibrium particle distribution function at point  $x$  and  $d^3\sigma_\mu(x)$  is the infinitesimal volume 4-vector normal to the freeze-out hypersurface at this point.

In this exploratory analysis, we concentrate on the longitudinal expansion and neglect, for simplicity, the effect of transverse expansion. We focus on the spectrum of pions – most abundant hadron species. We neglect quantum statistics in the phase space distribution – the generalization is straightforward. In this case  $f(p; u, T)$  is given by the Boltzmann distribution longitudinally boosted by fluid rapidity  $\alpha$ :

$$f(p; u, T) = e^{-\frac{p_\mu u^\mu}{T}} = e^{-\frac{m_\perp}{T} \cosh(Y-\alpha)}, \quad (2)$$

where  $m_\perp = \sqrt{p_\perp^2 + m_\pi^2}$  is the pion transverse mass,  $Y$  is the particle rapidity in the lab frame, related to the particle 4-momentum as

$$(p^t, p^z) = m_\perp (\cosh Y, \sinh Y) \quad (3)$$

and  $\alpha$  is the local fluid rapidity related to flow 4-velocity by

$$(u^t, u^z) = (\cosh \alpha, \sinh \alpha). \quad (4)$$

We parameterize the freeze-out hyper-surface using Bjorken coordinates  $\tau$  and  $\eta$

$$t = \tau \cosh \eta, \quad z = \tau \sinh \eta \quad (5)$$

by expressing the freeze-out proper time as a function of the Bjorken rapidity:  $\tau_f(\eta)$ . Using the expression for the hyper-surface volume element vector in the Bjorken coordinates:

$$(d^3\sigma_\tau, d^3\sigma_\eta) = \tau_f d\eta d^2x_\perp (1, -\partial_\eta \tau_f(\eta)) \quad (6)$$

we can write

$$p^\mu d^3\sigma_\mu = m_\perp \partial_\eta [\tau_f(\eta) \sinh(\eta - Y)] d\eta d^2x_\perp. \quad (7)$$

The local fluid rapidity  $\alpha$  is also a function of the Bjorken coordinate  $\eta$ . For example, purely Bjorken flow corresponds to  $\alpha(\eta) = \eta$ . We shall assume that this

function is monotonous, i.e., its inverse,  $\eta_f(\alpha)$ , is single-valued. The pion distribution in rapidity  $Y$  and transverse momentum  $p_\perp$  now reads:

$$\frac{d^3N}{dY d^2p_\perp} = \frac{A_\perp m_\perp}{(2\pi)^3} \int_{-\infty}^{\infty} d\alpha e^{-\frac{m_\perp}{T_f} \cosh(Y-\alpha)} \times \partial_\alpha [\tau_f(\alpha) \sinh(\eta_f(\alpha) - Y)], \quad (8)$$

where  $A_\perp$  is the total transverse area of the freeze-out hypersurface. We have changed the integration variable parameterizing the freeze-out surface from  $\eta$  to  $\alpha$  and used  $\tau_f(\alpha)$  as a shorthand for  $\tau_f(\eta_f(\alpha))$ . Integrating Eq. (8) by parts, we can write

$$\begin{aligned} \frac{d^3N}{dY d^2p_\perp} = & \frac{m_\perp^2}{(2\pi)^3 T_f} \int_{-\infty}^{\infty} d\alpha e^{-\frac{m_\perp}{T_f} \cosh(Y-\alpha)} \\ & \times \left( \sinh^2(Y-\alpha) \cdot [A_\perp \tau_f(\alpha) \cosh(\alpha - \eta_f(\alpha))] \right. \\ & \left. + \sinh(Y-\alpha) \cosh(Y-\alpha) \cdot [A_\perp \tau_f(\alpha) \sinh(\alpha - \eta_f(\alpha))] \right), \end{aligned} \quad (9)$$

where we enclosed the factors carrying information about the freeze-out surface (size, shape and flow velocity) in square brackets. These functions of  $\alpha$  will be important intermediate objects in our analysis, and we denote them as

$$\begin{aligned} \rho_1(\alpha) &\equiv A_\perp \tau_f(\alpha) \cosh(\alpha - \eta_f(\alpha)) = A_\perp \tau_f(\alpha) u_f^t(\alpha); \\ \rho_2(\alpha) &\equiv A_\perp \tau_f(\alpha) \sinh(\alpha - \eta_f(\alpha)) = A_\perp \tau_f^2(\alpha) u_f^z(\alpha) \end{aligned} \quad (10)$$

where we also note that they can be expressed in terms of the components of fluid velocity in Bjorken coordinates:

$$u^t = \cosh(\alpha - \eta), \quad u^z = \tau^{-1} \sinh(\alpha - \eta), \quad (11)$$

evaluated on the freeze-out surface parameterized by  $\alpha$ :  $\tau = \tau_f(\alpha)$ ,  $\eta = \eta_f(\alpha)$ .

The physical meaning of  $\rho_{1,2}$  can be understood as follows. The ratio

$$\rho_2/\rho_1 = \tanh(\alpha - \eta_f(\alpha)) \equiv v_\eta \quad (12)$$

is the local flow velocity, while  $\sqrt{\rho_1^2 - \rho_2^2} = A_\perp \tau_f(\alpha)$  is the volume per unit Bjorken rapidity both measured in the Bjorken frame at a given point on the freeze-out hypersurface.

Our first task is to reconstruct the freeze-out surface, i.e., to determine two independent functions:  $\tau_f(\alpha)$  and  $\eta_f(\alpha)$  appearing in Eq. (9) by matching Eq. (9) to experimentally observed particle spectrum. The direct inversion of Cooper-Frye freeze-out Eq. (9) is, of course, quite challenging. The quantity  $d^3N/dY dp_\perp^2$  measured in experiment is a result of a (linear) integral transform in Eq. (9) of functions  $\rho_{1,2}(\alpha)$  characterizing the shape of the freeze-out hyper-surface and the flow on it. This information about the freeze-out surface is blurred and distorted by the integral transformation.

Furthermore, as the number of points in particle rapidity space measured by experiments is typically smaller than the number of points needed in fluid rapidity space to characterize the freeze-out surface, i.e., the functions  $\rho_{1,2}(\alpha)$ , or  $\tau_f(\alpha), \eta_f(\alpha)$ , there would, in principle, be many different freeze-out surfaces which produce similar phase space particle distributions matching experimental data.

Fortunately, there exists a very well developed method for solving such a deconvolution problem – the maximum entropy method (MEM)[10]. In the spirit of the MEM, if there are many possible freeze-out surfaces in agreement with data, then the sensible question one could ask is what is the probability distribution and the measure in the space of all such freeze-out surfaces that takes into account the experimental data as well as our prior expectation of the freeze-out surface. If such probability distribution is given, the reconstructed freeze-out surface, i.e., the functions  $\tau_f(\alpha), \eta_f(\alpha)$ , can be obtained by averaging over all possible configurations weighted by the probability density. To make our paper self-contained, we provide a brief introduction to MEM in Appendix A.

We use the extended version of MEM[10, 14, 15] appropriate for the present purpose. With the aid of MEM, we reconstruct the longitudinal freeze-out surface, i.e., we find the “expectation value” for  $\rho_{1,2}$  and thus  $\tau_f(\alpha), \eta_f(\alpha)$  given the rapidity-dependent distribution measured by experiment. Those results are presented in detail in Sec. IV A. All technical details of maximum entropy reconstruction of freeze-out surface are summarized in Appendix B.

### III. GENERAL SOLUTIONS TO 1 + 1 IDEAL HYDRODYNAMICS

Once  $\tau_f(\alpha)$  and  $\eta_f(\alpha)$  are obtained (by MEM), our next task is to solve hydrodynamic equations and evolve the system back in time, from freeze-out to early times. It is convenient to change the coordinates in the hydrodynamic equations from  $t$  and  $z$  (or  $\tau$  and  $\eta$ ) to temperature  $T$  and fluid rapidity  $\alpha$ . Here,  $T$  and  $\alpha$  play the role of temporal and spatial variables respectively (e.g., in the Bjorken flow  $T$  is a function of  $\tau$  only and  $\alpha = \eta$ ). As a result, one could recast 1 + 1 ideal hydrodynamic equations into one *linear* second order differential equation, known as Khalatnikov equation [16]. For completeness, we shall first review the derivation of this equation following Belenkij and Landau[17]. After that, we shall study general solutions to that equation with Cauchy initial condition.

#### A. Khalatnikov equation

The relativistic ideal hydrodynamic equations we study are given by[18]:

$$(u^\mu \partial_\mu) \epsilon + (\epsilon + p) (\partial_\mu u^\mu) = 0, \quad (13a)$$

$$(\epsilon + p) (u^\nu \partial_\nu) u^\mu + (g^{\mu\nu} + u^\mu u^\nu) \partial_\nu p = 0, \quad (13b)$$

where  $\epsilon, p$  are the energy density and pressure respectively.  $u^\mu$  is the flow four-velocity that obeys  $u^\mu u_\mu = -1$ . Using thermodynamic relations  $d\epsilon = Tds, dp = sdT, \epsilon + p = Ts$ , where  $s$  is the entropy density, Eqs. (13) can be written as

$$\partial_\mu (s u^\mu) = 0, \quad (14a)$$

which is the conservation of entropy, and

$$u^\mu [\partial_\mu (T u_\nu) - \partial_\nu (T u_\mu)] = 0. \quad (14b)$$

– the relativistic analog of Euler equation.

For 1 + 1 dimensional flow we consider, Eqs. (14) become:

$$\partial_t (s u^t) + \partial_z (s u^z) = 0; \quad (15a)$$

$$\partial_t (T u_z) - \partial_z (T u_t) = 0. \quad (15b)$$

Due to Eq. (15b), one can introduce a potential  $\psi(t, z)$  such that

$$d\psi(t, z) = T u_t dt + T u_z dz = T(-\cosh \alpha dt + \sinh \alpha dz). \quad (16)$$

where we used  $\alpha$  defined in Eq. (4). To change the variables from  $t, z$  to  $T, \alpha$ , we now introduce a Legendre transform  $\psi(t, z)$  of the potential  $\chi(T, \alpha)$  as

$$\chi(T, \alpha) = \psi(t, z) - T u_t t - T u_z z \quad (17)$$

so that

$$\begin{aligned} d\chi(T, \alpha) &= -t d(T u_t) - z d(T u_z) \\ &= (t \cosh \alpha - z \sinh \alpha) dT \\ &\quad + T (t \sinh \alpha - z \cosh \alpha) d\alpha. \end{aligned} \quad (18)$$

The new potential,  $\chi(T, \alpha)$ , sometimes referred to as Khalatnikov potential, depends on  $T, \alpha$  only.

We then change the variables in Eq. (15a) from  $t, z$  to  $T, \alpha$ :

$$\begin{aligned} 0 &= \frac{\partial(t, z)}{\partial(T, \alpha)} \left[ \frac{\partial(s \cosh \alpha, z)}{\partial(t, z)} + \frac{\partial(s \sinh \alpha, t)}{\partial(z, t)} \right] \\ &= \frac{\partial(s \cosh \alpha, z)}{\partial(T, \alpha)} - \frac{\partial(s \sinh \alpha, t)}{\partial(T, \alpha)} \\ &= \frac{ds}{dT} \left[ -\frac{\partial t}{\partial \alpha} \sinh \alpha + \frac{\partial z}{\partial \alpha} \cosh \alpha \right] \\ &\quad - s \left[ -\frac{\partial t}{\partial T} \cosh \alpha + \frac{\partial z}{\partial T} \sinh \alpha \right], \end{aligned} \quad (19)$$

where  $\partial(t, z)/\partial(T, \alpha)$  denotes the Jacobian of the variable transformation from  $(t, z)$  to  $(T, \alpha)$ . Using Eq. (18) to simplify Eq. (19), we arrive at a second order linear partial differential equation for  $\chi(T, \alpha)$  [16, 17][19]

$$[c_s^2 T^2 \partial_T^2 + T \partial_T - \partial_\alpha^2] \chi(T, \alpha) = 0, \quad (20)$$

where  $c_s$  is the ( $T$ -dependent) speed of sound:

$$c_s^2 = \frac{dp}{d\epsilon} = \frac{sdT}{Tds}. \quad (21)$$

Once the potential  $\chi(T, \alpha)$  is found using Khalatnikov equation (20) one can determine  $\tau(T, \alpha)$  and  $\eta(T, \alpha)$  from the derivatives of  $\chi$ :

$$\partial_T \chi(T, \alpha) = \tau \cosh(\alpha - \eta) = \tau u^\tau; \quad (22a)$$

$$\partial_\alpha \chi(T, \alpha) = T\tau \sinh(\alpha - \eta) = T\tau^2 u^\eta, \quad (22b)$$

where we used Eqs. (18), (5) and (11).

To see how Khalatnikov equation (20) works, it is instructive to check it against known Bjorken solution in which  $\alpha = \eta$  or  $u^\eta = 0$ . On that solution,  $\chi$  is independent of  $\alpha$  according to Eq. (22b). Substituting  $\chi(T)$  into Eq. (20), one finds, for constant  $c_s$ ,  $\chi(T) = C_1 + C_2 T^{1-c_s^{-2}}$  where  $C_1, C_2$  are integration constants. Further substituting this into Eq. (22a), we have  $\tau \sim T^{-1/c_s^2}$  – the well-known result of Bjorken [1].

### B. The general solution of Cauchy problem for Khalatnikov equation

We now turn to the general solution of Eq. (20) with Cauchy initial condition on an isothermal hypersurface  $T(t, z) = \bar{T}$ . For simplicity, we shall consider the case of constant  $c_s$ . It is convenient to introduce a new variable

$$y = \log(T/\bar{T}). \quad (23)$$

It is also convenient to introduce a rescaled potential  $\bar{\chi}(y; \alpha)$ , related to  $\chi(T; \alpha)$  by

$$\chi(T; \alpha) = e^{-\nu y} \bar{\chi}(y; \alpha), \quad \text{where } \nu = \frac{1}{2} (c_s^{-2} - 1). \quad (24)$$

In terms of  $\bar{\chi}(y; \alpha)$ , the Khalatnikov equation takes the form of a massive Klein-Gordon equation:

$$(\partial_y^2 - c_s^{-2} \partial_\alpha^2 - \nu^2) \bar{\chi}(y; \alpha) = 0. \quad (25)$$

To solve Eq. (25), we introduce a Green's function  $G(y; \alpha)$  in terms of the modified Bessel function  $I_0$ ,

$$G(y; \alpha) = \frac{c_s}{2} I_0(\nu \sqrt{y^2 - c_s^2 \alpha^2}) \times [\theta(y - c_s \alpha) - \theta(-y - c_s \alpha)], \quad (26)$$

which satisfies Eq. (25) with the Cauchy initial condition

$$\lim_{y \rightarrow 0} G(y; \alpha) = 0, \quad \lim_{y \rightarrow 0} \frac{\partial G(y; \alpha)}{\partial y} = \delta(\alpha). \quad (27)$$

We note that  $G(y; \alpha)$  vanishes outside of the ‘‘sound horizon’’ at  $\alpha = \pm y/c_s$ . Solutions with given initial values of  $\bar{\chi}(y, \alpha)$  and  $\partial_y \bar{\chi}(y, \alpha)$  on the iso-thermal surface  $y = 0$  can then be found using  $G(y; \alpha - \alpha')$ :

$$\bar{\chi}(y, \alpha) = \int_{-\infty}^{\infty} d\alpha' [\bar{\chi}(0, \alpha') \partial_y + \partial_y \bar{\chi}(0, \alpha')] G(y; \alpha - \alpha'). \quad (28)$$

## IV. RESULTS

### A. Reconstructed freeze-out surface

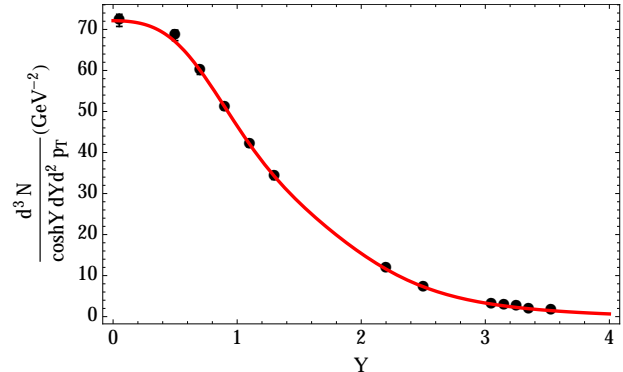


FIG. 1. (Color online) Charged pion rapidity distribution in central Au-Au collisions at  $\sqrt{s} = 200$  GeV in the  $p_\perp$  bin at  $p_\perp = 0.55$  GeV [2]. The experimental data errors are similar to the size of data points. The red curve is the rapidity distribution obtained from the MEM-reconstructed freeze-out surface (see Fig. 2 and text).

We first present our results on the MEM reconstruction of the longitudinal freeze-out surface and flow. Assuming the freeze-out temperature  $T_f = 140$  MeV, which is close to the one used in hydrodynamic simulations (e.g. [7, 8]), we have applied the maximum entropy method to the pion rapidity distribution measured in Au-Au central collisions at  $\sqrt{s} = 200$  GeV [2]. For this analysis we chose particles within the transverse momentum bin of width 0.1 GeV centered at  $p_\perp = 0.55$  GeV. This choice is motivated by the desire to minimize the effect of resonances (at lower  $p_\perp$ ) and viscous or non-hydrodynamic corrections (at higher  $p_\perp$ ).

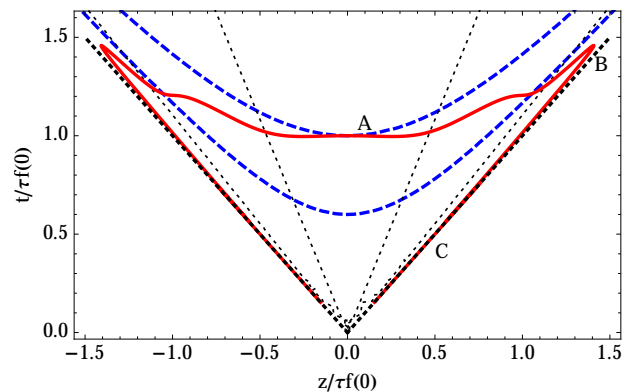


FIG. 2. (Color online) MEM-reconstructed freeze-out surface (red curve). Bjorken proper time  $\tau = \text{const}$  curves are dashed blue. Dotted rays correspond to Bjorken rapidities  $\eta = \pm 1, \pm 2$ . Letters A, B and C label characteristic points on the freezeout surface (see text and Fig. 3). The reconstruction uncertainties (not shown) are discussed in Appendix B.

The experimental data are plotted using black dots in Fig. 1. Applying the MEM to these data points, we obtain the reconstructed freeze-out surface shown in Fig. 2. As an important check, we also input the reconstructed freeze-out surface back into the Cooper-Frye formula (9) and compute the corresponding rapidity distribution. The result is shown in Fig. 1, indicating that our reconstructed freeze-out surface is consistent with the data.

In Fig. 2, we show the reconstructed freeze-out surface in  $t - z$  coordinates using the red solid curve. We rescaled dimensionful quantities such as  $t_f(\alpha), z_f(\alpha)$  by  $\tau_f(0)$  – the proper time at which the center of the fireball freezes out. As we have not included the dynamics of radial expansion in our analysis, we could only estimate the combination  $A_\perp \tau_f(0)$  rather than  $A_\perp$  and  $\tau_f(0)$  individually. We find  $A_\perp \tau_f(0) \approx (1.4 - 1.5) \times 10^4 \text{ fm}^3$  (somewhat large compared to typical values in hydrodynamic simulations).

The difference between our reconstructed freeze-out surface and idealized Bjorken’s boost-invariant model, where freeze-out occurs on an equal-proper-time hyperbola, is noticeable in Fig. 2. This difference is more clearly illustrated in Fig. 3 where freeze-out proper time  $\tau_f(\alpha)$  as a function of fluid rapidity  $\alpha$  is plotted as red solid curve. This plot shows that the mid-rapidity region of the fireball freezes out at later Bjorken proper times than the forward/backward rapidity regions.

Fig. 3 shows the longitudinal flow profile on the freeze-out surface. Since  $\alpha > \eta$ , the flow rapidity is faster than the idealized boost-invariant Bjorken scenario. This is expected, given the pressure gradients due to the pressure decreasing away from mid-rapidity. The effect in terms of  $|(\alpha - \eta_f)/\eta_f|$  is of the order of 10% – 20% for all  $\alpha$  we are considering.

Figure 3 could be thought of as a parametric representation of the freeze-out curve in  $t - z$  coordinates shown in Fig. 2. As the parameter  $\alpha$  increases from 0, the corresponding point in  $tz$  plane traces the curve from A to B to C. These points are also marked in Figure 3. For example, one can see that the increase of  $z$  from A to B and subsequent decrease from B to C is due to the competition between falling  $\tau(\alpha)$  and rising  $\eta(\alpha)$  in the formula  $z = \tau \sinh \eta$ .

We have, therefore, reconstructed hydrodynamic conditions on the freeze-out surface directly from the experimental data, remarkably, without using hydrodynamic simulations. We shall now take this result as the “initial” condition to evolve the system back in time.

## B. Temperature and flow history

We now present our results on the longitudinal evolution of the fireball. They are obtained by using the analytic solution to 1 + 1 ideal hydrodynamic equation, with Cauchy initial condition namely, Eq. (28). To use our knowledge on freeze-out surface, i.e.,  $\tau_f(\alpha), \eta_f(\alpha)$ , we

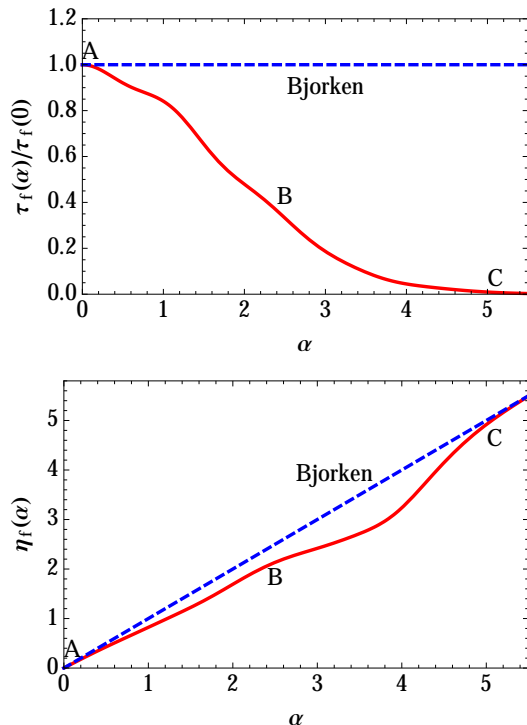


FIG. 3. (Color online) The shape,  $\tau_f(\alpha)/\tau_f(0)$ , and the flow profile,  $\eta_f(\alpha)$ , of the freeze-out surface found using MEM, as in Fig. 2, but represented parametrically in Bjorken coordinates. Letters A, B and C label characteristic points on the freeze-out surface and correspond to those in Fig. 2. Dashed blue lines show Bjorken’s boost-invariant approximation.

set  $\bar{T}$  to be  $T_f$  in our definition of  $y$ , i.e.,  $y = \log(T/T_f)$  in Eq. (28). The fact that the freeze-out surface is at  $T = \text{const}$  makes this boundary condition easy to set. As a result, we have from Eq. (22)

$$[-\nu \bar{\chi}(0; \alpha) + \partial_y \bar{\chi}(0; \alpha)] = T_f \tau_f(\alpha) \cosh(\alpha - \eta_f(\alpha)); \quad (29a)$$

$$\partial_\alpha \bar{\chi}(0; \alpha) = T_f \tau_f(\alpha) \sinh(\alpha - \eta_f(\alpha)). \quad (29b)$$

We then determine  $\bar{\chi}(0; \alpha)$  by integrating Eq. (29b) using  $\tau_f(\alpha)$  and  $\eta_f(\alpha)$  obtained by MEM reconstruction and shown in Fig. 3. In fact, as seen in Eqs. (10), the MEM directly outputs functions appearing in the r.h.s. of Eqs. (29a) and (29b). The integration constant is unphysical since  $\bar{\chi}(0, \alpha) = \chi(T_f, \alpha)$ , and potential  $\chi$  is defined up to a constant, Eqs. (16), (17). It can be fixed by requiring  $\bar{\chi}(0; \alpha) \rightarrow 0$  when  $\alpha \rightarrow \pm\infty$ . We next substitute the resulting  $\bar{\chi}(0; \alpha)$  into Eq. (29a) to obtain  $\partial_y \bar{\chi}(0; \alpha)$ . Consequently,  $\bar{\chi}(y; \alpha)$  for  $y > 0$  can be obtained from explicit solution Eq. (28). Finally, we read  $\tau(T, \alpha), \eta(T, \alpha)$  from resulting  $\chi = e^{-\nu y} \bar{\chi}$  using Eq. (22).

The longitudinal expansion history we find is summarized in Fig. 4. We used conformal equation of state  $c_s^2 = 1/3$ . We also checked that the output with a different choice of  $c_s^2$  is qualitatively similar.

Iso-thermal surfaces are shown as black solid curves in

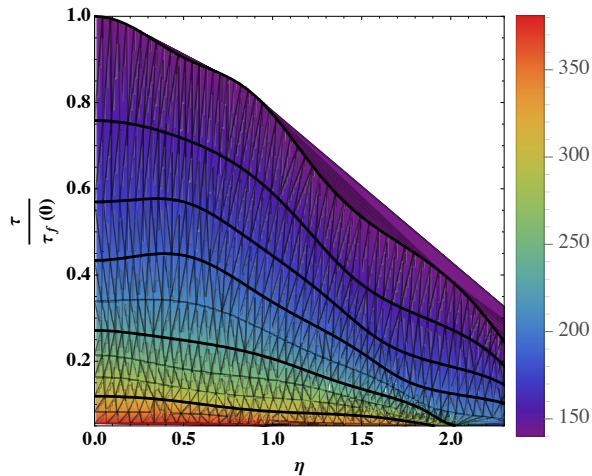


FIG. 4. (Color online) The temperature (in MeV) map in Bjorken coordinates. Solid contours denote iso-thermal surfaces.

Fig. 4. For comparison, Bjorken solution would correspond to horizontal isothermal contours on such a plot. We note that, even though the freeze-out (isothermal) surface has no visible plateau, the isothermal surfaces at higher temperatures (earlier times) do display a plateau which shrinks as the system evolves (cools down). We will comment more on this behavior later using different graphic representations.

It is interesting to compare the temperature (energy density) and flow profile at early (proper) time with initial conditions used in hydrodynamic simulations [5–8]. In such simulations initial energy profile is typically assumed to be flat around mid-rapidity with half a Gaussian fall-off in the forward and backward rapidity directions. Moreover,  $v_\eta$  is set to zero initially.

To facilitate the comparison, in Fig. 5, we plot equal proper time temperature profile,  $T$  vs  $\eta$ , and flow profile,  $v_\eta$  vs  $\eta$ , at early times:  $\tau = 0.4\tau_f(0)$ ,  $0.2\tau_f(0)$ , and  $0.1\tau_f(0)$ . In accordance with our observations in Fig. 4, the early-time temperature profile in Fig. 5 is qualitatively similar to the Bjorken-like plateau truncated at forward and backward rapidities used in hydrodynamic simulations [5–8]. In Fig. 5 one can also see that the flow is almost Bjorken-like ( $v_\eta \equiv \tanh(\alpha - \eta) \approx 0$ ) within the temperature plateau. In particular, the early-time profile we observe is much closer to Bjorken boost-invariant model ( $\alpha = \eta$ ), than to the full stopping assumption ( $\alpha = 0$ ).

Interestingly, at the earliest times we considered,  $v_\eta$  appears to be slightly negative (i.e.,  $\alpha < \eta$ ) within the plateau. Given the size of the uncertainties in the reconstruction of the flow (see bands on Fig. 5 and discussion below) we must interpret this result cautiously. It would be interesting to investigate this question further. Such a slower relative to Bjorken (Hubble-like) flow would be a natural consequence of the negative longi-

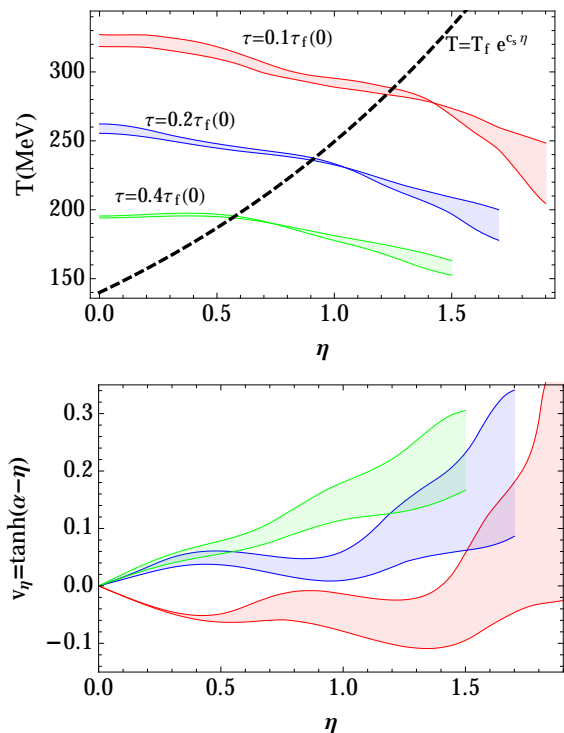


FIG. 5. (Color online) Temperature and flow profile on various equal-proper-time surfaces. Red, blue and green curves correspond to  $\tau = 0.1, 0.2, 0.4\tau_f(0)$  respectively. Shaded bands illustrate the initial condition dependence due to sensitivity to default model choice in MEM (see Appendix. B).

tudinal pressure in the pre-equilibrium glasma stage of heavy-ion collisions [20]. Early-time negative longitudinal pressure also occurs in holographic models of colliding shock waves [21], and has been observed in the “complex deformation” of the Bjorken flow studied in Ref. [22], where  $v_\eta < 0$  ( $\alpha < \eta$ ) can be also seen in its Fig. 2.

It is easy to see that the shrinking of the early-time Bjorken plateau follows the inward propagation of the shock waves from the plateau’s boundaries. Since the local velocity of the wave is  $c_s$ , it is easy to find that the wave propagates on top of the Bjorken flow in Bjorken coordinates according to  $d\eta/d\ln\tau = c_s$ . The length of the plateau shrinks linearly in  $\ln\tau$  at a rate of (twice) of  $c_s$ . Since, under Bjorken flow,  $T \sim \tau^{-c_s^2}$ , the edge of the plateau should follow  $T \sim e^{c_s\eta}$  in the  $T - \eta$  plot as illustrated by the dashed black curve in Fig. 5.

To estimate the sensitivity of our results to the uncertainty of the reconstruction of the freeze-out surface (“initial” conditions), we have reconstructed freeze-out surface using different choices of default models in MEM (see Appendix B) and evolved the output of such a reconstruction back in time. Shaded bands in Fig. 5 illustrate the difference due to the variation of default model. We observe that the temperature (energy density) profile due to the MEM reconstruction and back-in-time evolution is quite robust against the change of the default model. However, the uncertainty in the flow profile is

larger. Some more details on the default model dependence are given in Appendix. B.

## V. CONCLUSION

In this paper, we studied longitudinal expansion in heavy-ion collisions beyond Bjorken boost-invariant model. In contrast to existing body of work on the subject, we considered hydrodynamic evolution back in time – from freeze-out to earlier times. This is possible because we use experimental data directly to determine the starting point of the back-in-time evolution. To achieve that we applied the maximum entropy method to invert the Cooper-Frye freeze-out integral transformation relating the shape of the freeze-out hypersurface surface and the flow on it to rapidity distribution of observed particles. We use Khalatnikov-Landau approach to solve the longitudinal hydrodynamic Cauchy problem analytically.

We want to point out two remarkable facts, which together make our two-step approach natural and straightforward to implement. First, the transformation from the pair of functions  $\tau_f \cosh(\alpha - \eta_f) = \rho_1/A_\perp$  and  $\tau_f \sinh(\alpha - \eta_f) = \rho_2/A_\perp$  to experimentally observable  $d^3N/dYd^2p_\perp$  given by Eq. (9) is *linear*. Second, the same pair of functions translate linearly into the initial conditions, Eqs. (29), for the Khalatnikov equation which, in turn, is also linear.

By reconstructing the freeze-out surface and evolving the system back in time, we obtained both the temperature and the flow profile history of the longitudinal expansion. The temperature profile features a Bjorken-like plateau at early times. The plateau shrinks as the boundary shocks propagate inward, towards the center of the fireball (see Fig. 5). The flow velocity  $v_\eta$  with respect to local Bjorken frame remains small within the shrinking plateau (Fig. 5), i.e., the flow is close to being Bjorken-like (Hubble-like) inside the plateau: flow rapidity is close to Bjorken rapidity  $\alpha \approx \eta$ . The flow rapidity increases faster than Bjorken rapidity outside of the plateau ( $\alpha > \eta$  or  $v_\eta > 0$ ) due to pressure gradients.

We also observe the evidence that  $v_\eta < 0$  within the plateau at earlier times, which could represent the effect of the negative longitudinal pressure in pre-equilibrium glasma stage. These results provide useful information for determining the initial conditions for fully numerical hydrodynamic simulations as well as holographic models of heavy-ion collisions [23, 24].

In this first exploratory study of the new back-in-time

approach to fireball evolution, we attempted to achieve the most analytically transparent, yet phenomenologically meaningful results. For this reason, we focused on longitudinally expansion and neglected many other potentially important effects. Most notably, we neglected the dynamics of the transverse expansion and assumed temperature independent sound speed. Although not realistic, this is a common and useful approximation, successfully used since the seminal papers by Landau and Bjorken. Relaxing these approximations is, however, straightforward and extending the present approach to study the hydrodynamic expansion beyond longitudinal expansion would be an interesting direction to pursue.

We also neglected the effects of viscosity. Given the almost perfect fluidity of the quark-gluon plasma in the regime probed by heavy-ion collisions, the effect of viscosity should be small as far as bulk hydrodynamics we study is concerned. We believe that the advantage of analytical transparency afforded by the ideal hydrodynamic approximation more than compensates for the lack of numerical accuracy. Our goal is to provide useful insights for fully numerical hydrodynamic approaches aiming at quantitative precision.

One of the new ingredients in our analysis is the application of maximum entropy method (MEM). We found it to be a useful tool for inverting the Cooper-Frye freeze-out and reconstructing the freeze-out surface. As a general deconvolution method, MEM may also be used to reconstruct freeze-out surface in transverse plane or even full 3d freeze-out surface. The result of such a 2d or 3d reconstruction might reveal interesting information about the structure and evolution of the heavy-ion fireball.

## ACKNOWLEDGMENTS

The authors would like to express their gratitude to Paul Chesler, Ulrich Heinz, Dmitri Kharzeev, Denes Molnar, Wilke van der Schee, Edward Shuryak, Dam Son, Derek Teaney, Raju Venugopalan and Ho-Ung Yee for useful comments and discussions. Y.Y. would like to especially thank Todd Springer for stimulating conversations, Heng-Tong Ding for discussing MEM reconstruction, Kolja Kauder for explaining features of experimental measurements, and to acknowledge the lessons learned from the study of the lattice QCD MEM C-codes written by Pavel Buividovich. Y.Y. is grateful to UIC Dean's Scholar fellowship program for support. This research is supported by the US DOE grant No. DE-FG0201ER41195.

---

[1] J. Bjorken, *Phys.Rev.* **D27**, 140 (1983).  
 [2] I. Bearden *et al.* (BRAHMS Collaboration), *Phys.Rev.Lett.* **94**, 162301 (2005), [arXiv:nuclex/0403050](https://arxiv.org/abs/nuclex/0403050) [nucl-ex].

[3] B. Back, M. Baker, M. Ballintijn, D. Barton, B. Becker, *et al.*, *Nucl.Phys.* **A757**, 28 (2005), [arXiv:nuclex/0410022](https://arxiv.org/abs/nuclex/0410022) [nucl-ex].

- [4] E. Abbas *et al.* (ALICE Collaboration), (2013), arXiv:1304.0347 [nucl-ex].
- [5] L. Satarov, A. Merdeev, I. Mishustin, and H. Stoecker, *Phys.Rev.* **C75**, 024903 (2007), arXiv:hep-ph/0606074 [hep-ph].
- [6] P. Bozek and I. Wyslkiel, *Phys.Rev.* **C79**, 044916 (2009), arXiv:0902.4121 [nucl-th].
- [7] T. Hirano, K. Morita, S. Muroya, and C. Nonaka, *Phys.Rev.* **C65**, 061902 (2002), arXiv:nucl-th/0110009 [nucl-th].
- [8] B. Schenke, S. Jeon, and C. Gale, *Phys.Rev.* **C82**, 014903 (2010), arXiv:1004.1408 [hep-ph].
- [9] N. Wu, *The Maximum Entropy Method*, Data and Knowledge in a Changing World (Springer-Verlag, 1997).
- [10] R. Bryan, *European Biophysics Journal* **18**, 165 (1990).
- [11] F. Cooper and G. Frye, *Phys.Rev.* **D10**, 186 (1974).
- [12] M. Jarrell and J. Gubernatis, *Physics Reports* **269**, 133 (1996).
- [13] M. Asakawa, T. Hatsuda, and Y. Nakahara, *Prog.Part.Nucl.Phys.* **46**, 459 (2001), arXiv:hep-lat/0011040 [hep-lat].
- [14] A. T. Bajkova, *Astronomical and Astrophysical Transactions* **1**, 313 (1992).
- [15] H.-T. Ding, *Charmonium correlation and spectral functions in quenched lattice QCD at finite temperature*, Ph.D. thesis, Bielefeld University (2010).
- [16] I. Khalatnikov, *Zh.Eksp. Teor. Fiz.* **36**, 529 (1954).
- [17] S. Belenkij and L. Landau, *Nuovo Cim.Suppl.* **3S10**, 15 (1956).
- [18] L. Landau and E. Lifshits, *Fluid mechanics*, A-W series in advanced physics (Pergamon Press, 1959).
- [19] Equation. (20) has been applied to study longitudinal expansion in heavy-ion collisions in Ref. [25] recently.
- [20] T. Lappi and L. McLerran, *Nucl.Phys.* **A772**, 200 (2006), arXiv:hep-ph/0602189 [hep-ph].
- [21] D. Grumiller and P. Romatschke, *JHEP* **0808**, 027 (2008), arXiv:0803.3226 [hep-th].
- [22] S. S. Gubser, *Phys.Rev.* **C87**, 014909 (2013), arXiv:1210.4181 [hep-th].
- [23] P. M. Chesler and L. G. Yaffe, *Phys.Rev.Lett.* **106**, 021601 (2011), arXiv:1011.3562 [hep-th].
- [24] J. Casalderrey-Solana, M. P. Heller, D. Mateos, and W. van der Schee, *Phys. Rev. Lett.* **111**, 181601, 181601 (2013), arXiv:1305.4919 [hep-th].
- [25] A. Bialas, R. Janik, and R. B. Peschanski, *Phys.Rev.* **C76**, 054901 (2007), arXiv:0706.2108 [nucl-th]; G. Beuf, R. Peschanski, and E. N. Saridakis, *Phys.Rev.* **C78**, 064909 (2008), arXiv:0808.1073 [nucl-th]; R. Peschanski and E. N. Saridakis, *Nucl.Phys.* **A849**, 147 (2011), arXiv:1006.1603 [hep-th].
- [26] M. Hobson and A. Lasenby, (1998), arXiv:astro-ph/9810240 [astro-ph].
- [27] H. Jeffreys, *The Theory of Probability* (OUP Oxford, 1998).
- [28] The output of MEM typically contains wiggles – a known artifact of the method [15]. We applied a moving average filter to suppress them.

## Appendix A: A brief review of the maximum entropy method

In this section, we briefly review essential details of the maximum entropy method (MEM) used in the present paper to reconstruct the freeze-out surface. For further details and explanation an interested reader may refer to review[13] or textbook[9].

Let us begin by putting the Cooper-Frye integral transformation Eq. (9) into the following form:

$$n_{\text{th}}(Y) = \int_0^\infty d\alpha [K_1(Y; \alpha)\rho_1(\alpha) + K_2(Y; \alpha)\rho_2(\alpha)] , \quad (\text{A1})$$

where  $n_{\text{th}}(Y) \equiv (dN/dY)_{\text{th}}$  denotes the theoretically expected particle rapidity distribution given freeze-out surface size, shape and flow encoded in functions  $\rho_{1,2}(\alpha)$  defined in Eq. (10). Here,

$$K_1(Y; \alpha) = \frac{m_\perp^2}{(2\pi)^3 T_f} \left[ e^{-\frac{m_\perp}{T_f} \cosh(Y-\alpha)} \times \sinh^2(Y-\alpha) + (\alpha \rightarrow -\alpha) \right] ; \quad (\text{A2a})$$

$$K_2(Y; \alpha) = \frac{m_\perp^2}{(2\pi)^3 T_f} \left[ e^{-\frac{m_\perp}{T_f} \cosh(Y-\alpha)} \times \sinh(Y-\alpha) \cosh(Y-\alpha) - (\alpha \rightarrow -\alpha) \right] . \quad (\text{A2b})$$

are kernels directly determined from Eq. (9) and we used  $\rho_1(\alpha) = \rho_1(-\alpha)$  and  $\rho_2(\alpha) = -\rho_2(-\alpha)$ .

The standard  $\chi^2$  fit to reconstruct the “image” functions  $\rho_1(\alpha), \rho_2(\alpha)$  from the data  $n_{\text{exp}}$  amounts to minimizing the usual likelihood functional:

$$E(\rho_1, \rho_2) \equiv \frac{1}{2} \sum_{Y, Y'} C^{-1}(Y, Y') [n_{\text{th}}(Y) - n_{\text{exp}}(Y)] \times [n_{\text{th}}(Y') - n_{\text{exp}}(Y')] . \quad (\text{A3})$$

Here,

$$C(Y, Y') \equiv \langle [n_{\text{th}}(Y) - n_{\text{exp}}(Y)] [n_{\text{th}}(Y') - n_{\text{exp}}(Y')] \rangle \quad (\text{A4})$$

is the “covariance matrix” characterizing expected deviations between the theoretical model and the experimental results. Typically the number of the data points is smaller than that needed to adequately characterize  $\rho_1(\alpha), \rho_2(\alpha)$ . As a result, there are infinitely many minima of the likelihood functional, or “energy”,  $E(\rho_1, \rho_2)$  in  $\rho_1, \rho_2$  space – there are flat directions in that space. A sensible question one may ask in order to lift this degeneracy would be: what is the probability distribution of  $\rho_{1,2}$  given the data as well as our prior estimation  $m_1, m_2$  of  $\rho_1, \rho_2$ ? We can express this probability as

$$P_\beta(\rho_1, \rho_2 | m_1, m_2) = e^{-\beta F_\beta(\rho_1, \rho_2; m_1, m_2)} . \quad (\text{A5})$$



Here, the “free energy” contains the likelihood functional  $E$  and the entropy functional  $S$ :

$$\beta F_\beta = S(\rho_1, \rho_2; m_1, m_2) - \beta E(\rho_1, \rho_2). \quad (\text{A6})$$

The “inverse temperature”  $\beta$  here will balance the relative importance between the data (given by the “energy term”  $E$ ) and our prior estimate (“entropy term”  $S$ ).

Assuming no correlation between  $\rho_1, \rho_2$ , we can write  $S(\rho_1, \rho_2)$  as

$$S(\rho_1, \rho_2) = S_1(\rho_1) + S_2(\rho_2). \quad (\text{A7})$$

For the case at hand where  $\rho_1(\alpha) = A_\perp \tau_f(\alpha) u_f^\tau(\alpha)$  is positive definite and the sign of  $\rho_2(\alpha) = A_\perp \tau_f(\alpha) u_f^\eta(\alpha)$  can, in principle, be either positive or negative, we have:

$$S_1(\rho_1) = \int_0^\infty d\alpha \left[ \rho_1(\alpha) - m_1(\alpha) - \rho_1(\alpha) \log \frac{\rho_1(\alpha)}{m_1(\alpha)} \right], \quad (\text{A8a})$$

$$S_2(\rho_2) = \int_0^\infty d\alpha \left[ \sqrt{\rho_2^2(\alpha) + 4m_2^2(\alpha)} - 2m_2(\alpha) - \rho_2(\alpha) \log \frac{\sqrt{\rho_2^2(\alpha) + 4m_2^2(\alpha)} + \rho_2(\alpha)}{2m_2(\alpha)} \right]. \quad (\text{A8b})$$

Both expressions for the entropy Eq. (A8a) and Eq. (A8b) are derived using the law of large numbers (see Ref. [13] for example for the derivation of Eq. (A8a) and Ref. [26] for Eq. (A8b)). Eq. (A8a) is the standard Shannon-Jaynes entropy used for reconstructing arbitrary positive function (e.g., spectral density in lattice applications [13]) and Eq. (A8b) is the extended version of the Shannon-Jaynes entropy used for reconstructing image function whose sign is indefinite [15, 26]. The form of  $S(F_1, F_2)$  adapted here, i.e., Eqs. (A7) has been applied to deconvolute *complex* image functions previously [14].

Given the probability distribution in Eq. (A5) we can determine an expectation value as a “weighted average” of the image functions  $\rho_{1,2}$ :

$$\rho_{1,2}^{\text{MEM}}(\alpha) = \langle \rho_{1,2}(\alpha) \rangle \equiv Z^{-1} \int \frac{d\beta}{\beta} \int \mathcal{D}\rho_1(\alpha) \mathcal{D}\rho_2(\alpha) \times e^{-\beta F_\beta(\rho_1, \rho_2; m_1, m_2)} \rho_{1,2}(\alpha), \quad (\text{A9})$$

where, rather than picking a particular value for  $\beta$ , we followed a commonly used Jeffreys’ rule [27] and integrated over a scale-invariant measure  $d\beta/\beta$ . The normalization constant  $Z$  is fixed by requiring  $\langle 1 \rangle = 1$ .

## Appendix B: Maximum entropy reconstruction of the freeze-out surface.

In practice, the functional integral in Eq. (A9) is evaluated in the saddle point approximation. The saddle point

$\rho_1, \rho_2$  is determined by minimizing  $\beta F_\beta(\rho_1, \rho_2)$ :

$$\frac{\delta F_\beta(\rho_1, \rho_2)}{\delta \rho_1} = 0, \quad \frac{\delta F_\beta(\rho_1, \rho_2)}{\delta \rho_2} = 0. \quad (\text{B1})$$

As one can show, for example along the lines of Ref. [13], the solution to Eq. (B1) is unique if it exists. The contribution of configurations close to the saddle point is included by approximating  $F_\beta$  by a Gaussian. We have developed a Mathematica package incorporating Bryan’s algorithm [10] to find  $\rho_{1,2}(\alpha)$  minimizing  $\beta F_\beta(\rho_1, \rho_2)$  and to evaluate  $\rho_{1,2}^{\text{MEM}}(\alpha)$  as given by Eq. (A9).

As explained in Sec. IV A, rapidity-dependent pion distribution is taken from Au-Au collision data at  $\sqrt{s} = 200$  GeV [2]. For simplicity, we assume the covariance matrix is diagonal with relative errors of 3 percent that  $C(Y, Y') \approx (0.03 n_{\text{exp}}(Y))^2 \delta_{Y, Y'}$ . Incorporating a more elaborate covariance matrix is straightforward. To calculate functional derivative Eq. (B1) numerically, we also discretize fluid rapidity space from 0 to  $\alpha_{\text{max}} = 6$  into 60 equally-spaced pixels with spacing  $\Delta\alpha = 0.1$ . Our choice of spacing  $\Delta\alpha = 0.1$  in fluid rapidity space is guided by the actual spacing in the spatial rapidity space used by such hydrodynamic simulations as Ref. [8].

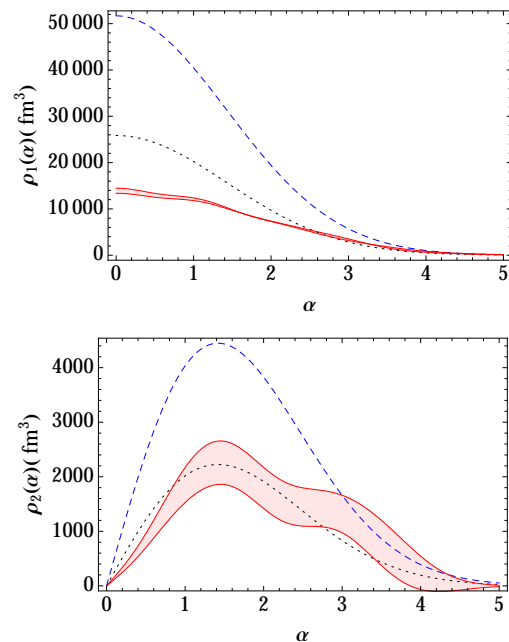


FIG. 6. (Color online) The default model dependence of MEM reconstruction. Bands shown here are obtained by taking different default models (blue and black dashed lines). (a):  $A_\perp \tau_f(\alpha) u_f^\tau(\alpha)$  or  $\rho_1(\alpha)$ . (b):  $A_\perp \tau_f^2(\alpha) u_f^\eta(\alpha)$  or  $\rho_2(\alpha)$ .

Motivated by the results of previous hydrodynamic simulations [5, 6], we parameterize our prior estimate of  $\tau_f(\alpha), \alpha_f(\alpha)$  by three parameters  $a, b, c$

$$A_\perp \tau^{\text{prior}}(\alpha) = a e^{-b\alpha^2}, \quad \alpha - \eta^{\text{prior}}(\alpha) = c\alpha \quad (\text{B2})$$

where  $\tau^{\text{prior}}, \eta^{\text{prior}}$  are related to default models in

Eq. (A8) by

$$m_1(\alpha) = A_{\perp} \tau^{\text{prior}}(\alpha) \cosh(\alpha - \eta^{\text{prior}}(\alpha)); \quad (\text{B3a})$$

$$m_2(\alpha) = A_{\perp} \tau^{\text{prior}}(\alpha) \sinh(\alpha - \eta^{\text{prior}}(\alpha)). \quad (\text{B3b})$$

We have checked the default model dependence of MEM reconstruction with various choices of  $(a, b, c)$ . To provide a transparent idea of the sensitivity of our results to the choice of default model, in Fig. 6, we have plotted the output of the maximum entropy method  $\rho_1(\alpha), \rho_2(\alpha)$  for two different choices of  $a$  and fixed  $b, c$ . [28]. The error

band in Fig. 5 is based on results of our analysis using those two default models. From Fig. 6, we notice that  $\rho_1(\alpha)$  reconstructed using the maximum entropy method is relatively insensitive to the choice of the default model. This can be understood as a consequence of the fact that the error bars on the data are small and about 80 – 90% of the contribution to  $dN/dY$  comes from  $\rho_1(\alpha)$ . On the other hand, since the contribution of  $\rho_2(\alpha)$  to  $dN/dY$  is much smaller, the data constrains  $\rho_2(\alpha)$  much less, and thus the sensitivity to the choice of the default model is stronger, as seen in Fig. 6.